Bulk Heterojunction Organic Photoanodes for Enhanced Water Oxidation and Unassisted Solar Water Splitting

Matyas Daboczi[1,], Flurin Eisner[2,3,*], Joel Luke[2], Shi Wei Yuan[2], Noof Al Lawati[1], Jolanda Simone Müller[2], Ji-Seon Kim[3], Jenny Nelson[2,*], Salvador Eslava[1,*]*

[1] Department of Chemical Engineering and Centre for Processable Electronics, Imperial College London, London SW7 2AZ, UK

[2] Department of Physics and Centre for Processable Electronics, Imperial College London, London SW7 2AZ, UK

[3] Department of Materials, Imperial College London, London SW7 2AZ, UK

*e-mail: m.daboczi@imperial.ac.uk; f.eisner15@imperial.ac.uk; jenny.nelson@imperial.ac.uk; s.eslava@imperial.ac.uk

---

Abstract

Polymer donors and non-fullerene acceptors have played an important role as photoactive materials in the development of high-efficiency organic solar cells, and they have immense potential for photoelectrochemical generation of solar fuels such as green hydrogen. However, their use in water-splitting photoelectrodes has been limited by their instability in aqueous environment and recombination losses at the interface with catalysts. Herein, PM6:D18:L8-BO organic photoanodes are presented reaching high photocurrent density over 25 mA cm^{-2} at +1.23 V_{RHE} and unprecedented, days-long operational stability under solar illumination. This photoelectrochemical performance was achieved by protecting the photoactive layer by a graphite sheet functionalized with earth-abundant NiFeOOH water oxidation catalyst, providing both water resistance and electrical connection between the catalyst and the photoactive layer without any losses. This strategy also enables unassisted solar water splitting with solar-to-hydrogen efficiency of 5% by monolithic tandem organic photoanodes with PM6:D18:L8-BO and PTQ10:GS-ISO photoactive layers. These results pave the way towards high-efficiency, stable and unassisted hydrogen generation by low-cost organic photoelectrochemical cells.

Keywords: organic semiconductor, photoanode, solar fuel, water splitting, days-long stability.

One of the most pressing challenges in achieving net zero is the production of inexpensive low-emission fuels.[1] Among different sustainable fuel production technologies, direct solar water splitting is a promising route towards off-grid, low-cost hydrogen production with low environmental footprint.[2] In particular, solar water splitting using photoelectrochemical (PEC) cells or photocatalytic reactors has the potential for very low system costs and for using sustainable materials and production methods, with PEC approaches thus far offering the greater potential for achieving high solar-to-hydrogen (STH) efficiencies.[3,4] However, existing PEC systems based on inorganic semiconductors have thus far failed to achieve the combination of high performance, long-term stability, low manufacturing costs and use of earth-abundant materials necessary for large-scale deployment.[5,6]

Organic semiconductors have emerged as efficient material systems for converting sunlight into electricity in photovoltaic cells and are compatible with eco-friendly and low-cost large-scale manufacturing methods.[7–9] In theory, organic semiconductors are also promising candidates for efficiently driving PEC reactions, as their tunable optical and electronic properties allow them to be tailored to suit the specific PEC requirements.[10–12] Organic semiconductors have thus gained wide-spread interest for driving water-splitting reactions in PEC systems. The most promising approaches so far have adopted the donor-acceptor bulk heterojunction (BHJ) approach used in organic photovoltaic (OPV) devices and encouraging progress has been achieved on both BHJ photocathodes and photoanodes.[13–18] However, despite these promising demonstrations, there has been limited success in translating the high photocurrent densities (j_{ph}) achievable in BHJ OPV devices (> 25 mA cm^{-2}) into PEC cells (2-15 mA cm^{-2}). Reaching high j_{ph} in organic BHJ photoanodes is still to be achieved, especially in conjunction with operational PEC stability at least on the order of days.[18,19]

A major challenge to improving solar-to-fuel conversion efficiencies in organic PEC cells is minimizing electronic losses between the photo-absorbing organic semiconductor and the electrocatalysts that are deposited on the organic layer, in most cases to efficiently catalyze either water oxidation or reduction.[14,15,19] This is particularly important for photoanodes, where the sluggish oxidation reaction kinetics can lead to rapid build-up of charges at the organic semiconductor/electrocatalyst interface that decrease efficiency and lead to degradation of the organic semiconductor.[10,14] Previous efforts to address this have included using polymer[14,16] or metal-oxide[20,21] interlayers, as well as more elaborate (and expensive) encapsulation techniques.[17]

Here, we present organic BHJ photoanodes that apply a straightforward, cost-effective approach to simultaneously prevent degradation by the aqueous environment and eliminate almost all electrical losses between the highly efficient BHJ photoactive layer and the water oxidation-catalyst. The developed single-junction photoanode containing a polymer:non-fullerene acceptor absorber and a self-adhesive graphite sheet functionalized by earth-abundant nickel–iron oxyhydroxide (NiFeOOH) electrocatalyst achieves water oxidation with breakthrough j_{ph} of over 25 mA cm^{-2} at +1.23 V vs. reversible hydrogen electrode (V_{RHE}) and remarkable, days-long operational stability. Moreover, the universality of the approach enables the demonstration of high-efficiency polymer:polymer photoelectrodes, as well as monolithic organic tandem photoanodes with a negative onset potential (E_{on}) of –0.41 V_{RHE} and unassisted (*i.e.*, bias-free) solar water splitting in a two-electrode setup showing a remarkable 5% STH efficiency.

Fabrication of organic photoanodes

The schematic structure of the fabricated organic photoanodes and the related energy band diagrams and chemical composition of the materials used in optimized devices are shown in Fig. 1. In the optimized devices, SnO_2 electron transport layer (ETL) and MoO_3 hole transport layer (HTL) were used. The organic photoactive layer comprises a ternary blend of PM6 and D18 donor polymers, absorbing in the 400-700 nm wavelength range due to their relatively large optical bandgaps (1.9 and 2.1 eV, respectively), and L8-BO, a non-fullerene acceptor absorbing light up to 900 nm due to its narrow optical bandgap (1.45 eV). The top of the photoanodes consist of a 70 µm thick graphite sheet functionalized with NiFeOOH on the front side and adhesive on the back side. This sheet is attached directly to the thin (30 nm) top MoO_3/gold contact of the photoactive layer and serves simultaneously as a water resistant and electrically conductive protective layer and electrocatalyst. The graphite sheet has highly oriented layers and large porosity (10-50 µm pores, 50% porosity) providing large surface area for the electrodeposition of the NiFeOOH electrocatalyst.[22]

The highest occupied molecular orbital (HOMO) and Fermi level values of the separate device layers were measured by ambient photoemission spectroscopy (Supplementary Fig. 1) and Kelvin probe (Supplementary Fig. 2), respectively. The energy level of the lowest unoccupied molecular orbital (LUMO) for the organic semiconductors were calculated using the HOMO and the optical bandgap values to construct the energy band diagrams of all constituent layers of the photoanode (Fig. 1c). Importantly, the HOMO of both donor polymers (–5.05 eV) lie deeper than the theoretical electrochemical potential of water oxidation at pH 14 (–4.90 eV), a thermodynamic requirement for water oxidation and an advantage for low E_{on} of photoanodes.

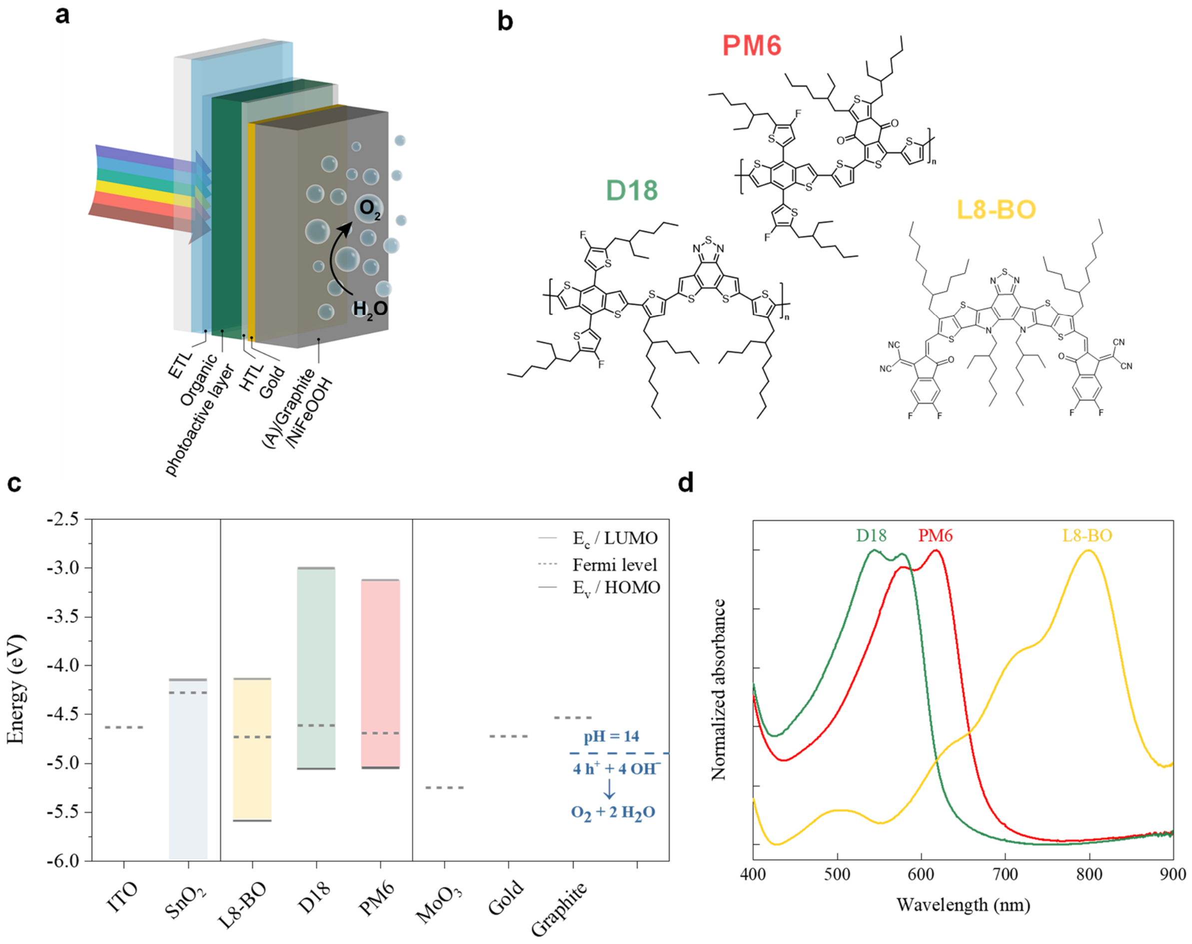

Fig. 1 | Structure, composition, and energetics of PM6:D18:L8-BO organic photoanodes. **a,** Schematic representation of the water oxidation photoanode containing an organic photoactive layer and a self-adhesive (A) graphite sheet as a conductive protection layer (not to scale). The adhesive layer is not shown as there is direct electrical contact between the gold and graphite layers. **b,** Chemical structures of PM6, D18 and L8-BO, the three photoactive materials in the ternary bulk heterojunction blend. **c,** Energy level diagrams for all constituent layers of the organic photoanode. The blue dashed line indicates the electrochemical potential of water oxidation to oxygen at pH 14. **d,** Normalized absorbance spectra of PM6, D18 and L8-BO.

PEC performance of organic photoanodes

The successful electrodeposition of the NiFeOOH electrocatalyst on the graphite sheet was confirmed by a more than 500 mV cathodic shift in E_{on} for water oxidation at pH 14 (Supplementary Fig. 3). These functionalized graphite sheets were attached to the thin metal electrode of OPVs including a PM6:D18:L8-BO photoactive layer and various HTLs and ETLs (Supplementary Fig. 4 and Supplementary Fig. 5). We found that SnO_2 ETL and MoO_3 HTL yielded the highest j_{ph} at +1.23 V_{RHE}, plausibly due to the improved charge carrier extraction and higher photovoltage resulting in a reduced E_{on}. The increased photovoltage is also reflected in the larger change in open circuit potential (ΔOCP) of the photoanodes upon switching off the 1 sun illumination compared to dark (Supplementary Fig. 4 and Supplementary Fig. 5). The optimized 0.28 cm^2 active area organic photoanodes showed a champion j_{ph} of 26.4 mA cm^{-2} (average of 23.8 ± 2.1 mA cm^{-2}) at +1.23 V_{RHE} and an E_{on} as low as +0.66 V_{RHE} (average of +0.69 ± 0.02 V_{RHE}) both under continuous and chopped 1 sun illumination, in aqueous 1 M NaOH electrolyte at pH 14 (Fig. 2a,b). E_{on} was determined conservatively by linear fitting of the photocurrent rise. The saturation of j_{ph} above +1.4 V_{RHE} was confirmed by subtracting the dark current density from the current density under 1 sun illumination (Supplementary Fig. 6). The photoanodes generated stable j_{ph} above 20 mA cm^{-2} even with the use of a UV filter (Fig. 2c), which was applied for enhanced long-term stability, as discussed later. The short-circuit current density (J_{sc}) of solar cells up to 26.8 mA cm^{-2} (Fig. 2b) agrees well with the high j_{ph} measured in the photoanodes (26.4 mA cm^{-2}) and is the highest reported j_{ph} value considering all single-junction solution-processed semiconductor photoanodes. The open circuit voltage (V_{oc}) of 0.90 V recorded for the organic solar cell devices is also in good agreement with the ΔOCP of 0.85 V measured for the photoanodes (Supplementary Fig. 5).

Recombination losses in the organic solar cells with and without the top graphite sheet were investigated by light intensity dependent V_{oc} (Fig. 2d) and J_{sc} (Supplementary Fig. 7) measurements. Deposition of the graphite sheet had minimal effect on the light intensity dependence of solar cells, which suggests the elimination of most electrical losses between the top electrode of the organic BHJ solar cell and the catalyst-functionalized graphite sheet. The negligible impact of the graphite sheet on OPV operation was also confirmed by measuring the organic photoanodes with and without the graphite sheet as solar cells, showing almost identical electroluminescence, external quantum efficiency spectra (Supplementary Fig. 8), current-voltage curves (Supplementary Fig. 9), and voltage losses (Supplementary Table 1). These results show that the pre-deposited adhesive layer at the back of the graphite sheet is thin and/or discontinuous enough to ensure direct electrical contact between the rough graphite sheet and the Au top electrode; therefore, no conductive fillers are needed in the adhesive layer.[23] Importantly, these results demonstrate that the addition of the graphite sheet with its adhesive and NiFeOOH layers does not significantly impact charge recombination.

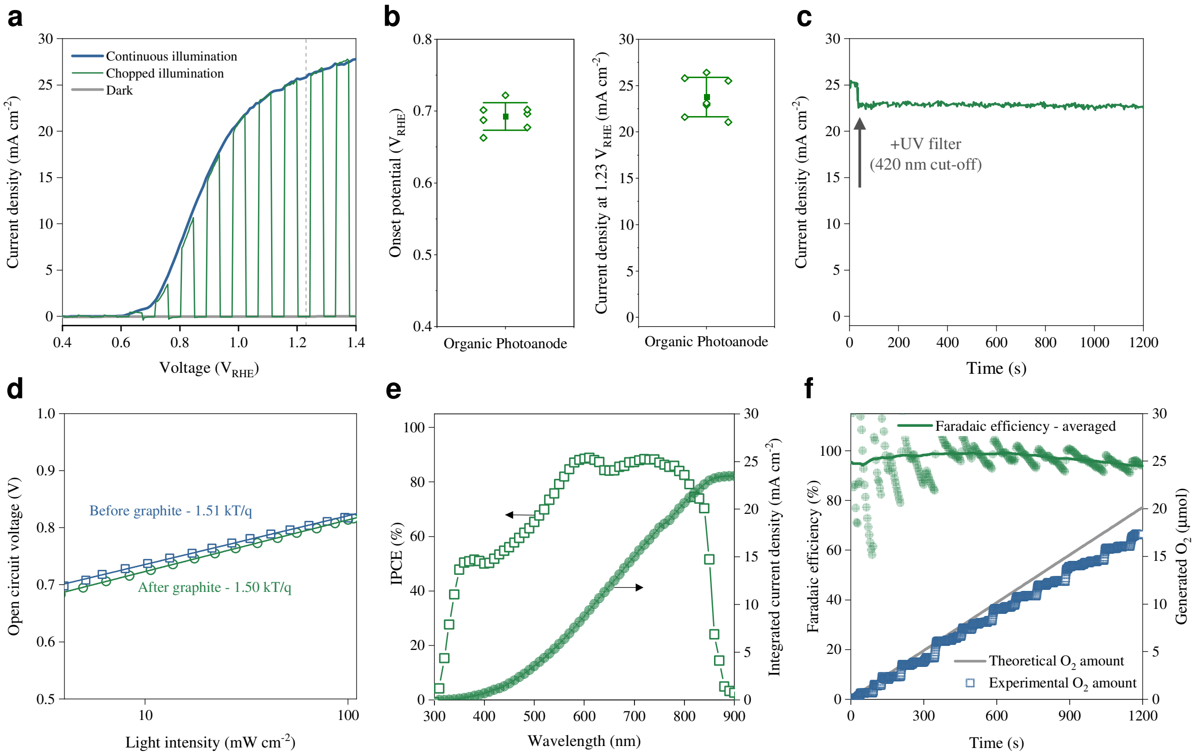

Fig. 2 | PEC performance of PM6:D18:L8-BO organic photoanodes with 0.28 cm^2 active area. a, Current–voltage scans in the dark, under 1 sun continuous and chopped illumination for a high-performing PM6:D18:L8-BO photoanode. Scan rates were 20 mV s^{-1} for chopped illumination and 50 mV s^{-1} for the rest. Dashed vertical line at +1.23 V_{RHE} indicates the standard oxidation potential of water to oxygen. **b,** Box plots of the onset potentials and photocurrent densities at +1.23 V_{RHE} extracted from the current–voltage scans of 7 organic photoanodes from different batches. Open diamond symbols show the values measured for the individual devices (lateral displacement is only for clarity), the solid squares are the mean values, and the whiskers represent one standard deviation. **c,** Stabilized photocurrent density of a representative PM6:D18:L8-BO photoanode under 1 sun illumination without (0 – 30 s) and with (30 – 1200 s) a 420 nm cut-off UV filter. **d,** Light intensity dependent open circuit voltage of the organic photoanode before and after deposition of the top graphite sheet. **e,** IPCE spectra and integrated photocurrent density at +1.23 V_{RHE} of a representative organic photoanode. **f,** Faradaic efficiency of an organic photoanode calculated from the measured amount of generated O_2 compared to the theoretical amount of O_2 based on the recorded photocurrent. The PEC measurements were performed in an aqueous 1 M NaOH electrolyte.

A further necessary requirement to achieve high j_{ph} is the preparation of uniform, pinhole-free photoactive layers with high shunt resistance (measured between the bottom ITO and top graphite sheet electrodes in this case). We found that increasing the thickness of the photoactive layer from around 110 nm (the optimum for solar cells) to above 200 nm significantly enhanced PEC performance by increasing shunt resistance (Supplementary Fig. 10). The relatively large standard deviation (± 2.1 mA cm^{-2}) of j_{ph} measured at +1.23 V_{RHE} for 7 devices from different batches (Supplementary Fig. 11) is potentially due to the effect of varying active layer uniformity and resistance, especially for larger (0.28 cm^2) devices. The statistical analysis of smaller area (0.05 cm^2) OPV also shows a similar trend: small variation in V_{oc} (0.89 ± 0.01 V), but larger in J_{sc} (25.1 ± 0.9 mA cm^{-2}) and fill factor (0.63 ± 0.03) (Supplementary Fig. 12), suggesting that the effect of active layer uniformity and shunt resistance is also present in the solar cells. Overall, the statistical analysis of photoanodes and solar cells confirm the high j_{ph} achieved close to the theoretical limit (~ 31 mA cm^{-2}) of the applied PM6:D18:L8-BO photoactive layer with an optical bandgap of 1.45 eV.[24] Accordingly, the incident photon-to-current efficiency (IPCE) at +1.23 V_{RHE} of the organic photoanodes reached close to 90% in the 600–800 nm wavelength range with an integrated product of IPCE, unit charge and AM 1.5G solar spectrum of 23.5 mA cm^{-2} (Fig. 2e), in good agreement with the average j_{ph} of 23.8 mA cm^{-2} measured under 1 sun illumination. The amount of generated O_2 gas during continuous operation on this photoanode was measured and compared to the theoretical amount of O_2 calculated from the recorded photocurrent, yielding a high Faradaic efficiency of 97% (Fig. 2f).

To show the universality of the approach, polymer:polymer photoanodes were also fabricated with an organic photoactive layer consisting of PM6 and PY-IT. The polymer:polymer photoanodes also achieved a high average j_{ph} of 23.3 mA cm^{-2} at +1.23 V_{RHE} and an E_{on} of +0.63 V_{RHE}, which is 60 mV improvement compared to the ternary PM6:D18:L8-BO devices (Supplementary Fig. 13). The lower E_{on} is in accordance with the higher photovoltage indicated by ΔOCP measurements (Supplementary Fig. 13), which is plausibly due to the different energetics of PY-IT compared to L8-BO (Supplementary Fig. 1).

Differences between PEC and solar cell operation

To gain insight into the operation and losses of the organic photoanodes, light intensity dependent measurements were performed on the devices as photoanodes and solar cells (Fig. 3). The j_{ph} of organic photoanodes at +1.23 V_{RHE} and the J_{sc} of organic solar cells both show a linear relationship on a log-log scale against the light intensity. This relationship remains true for the full range of light intensities for the solar cells; however, the j_{ph} of the photoanodes fall below the power-law fit at light intensities smaller than 30 mW cm^{-2} (Fig. 3b, e). This implies increased recombination in the photoanodes at lower photogenerated charge carrier densities, possibly originating from the electrocatalyst/electrolyte interface. A similar trend is observed in the photoanode ΔOCP and solar cell V_{oc} with light intensity (Fig. 3c, f). The light intensity dependence of V_{oc} again shows a linear relationship on a log-log scale for the organic solar cells with a slope of $1.5kT/q$ (meaning a light ideality factor of 1.5), where kT is the thermal energy and q is the elementary charge. However, the relationship of the ΔOCP of photoanodes and the light intensity follows the power-law fit only at high light intensities (>30 mW cm^{-2}) and present a larger slope of 3.3kT/q, which suggests increased recombination in the organic photoanodes compared to the solar cells.[25,26] We note that the reaction kinetics might also change under varied illumination intensities; however, as the ΔOCP measurements were performed at the same low j_{ph} (~10^{-8} mA cm^{-2}), reaction kinetics is plausibly a less significant effect here.

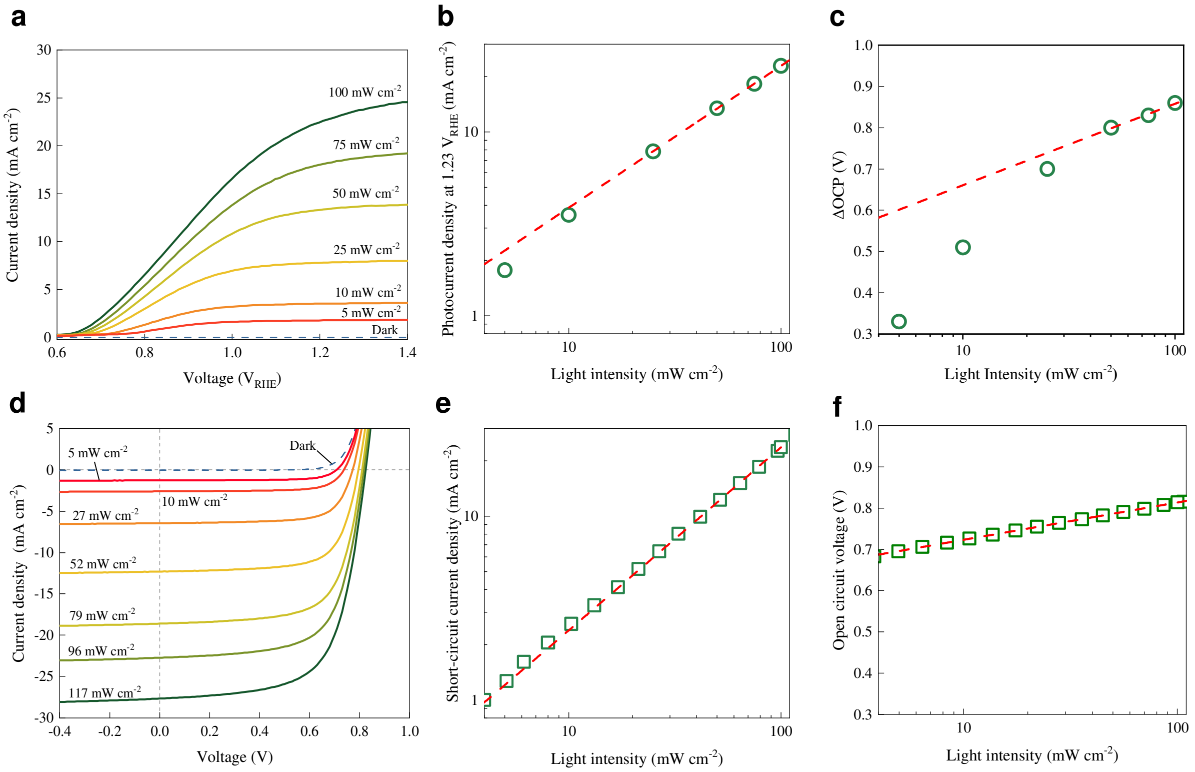

Fig. 3 | Light intensity dependence of PM6:D18:L8-BO organic photoanodes and solar cells. a, Current–voltage scans of the PM6:D18:L8-BO photoanode at different light intensities measured in aqueous 1 M NaOH electrolyte at 50 mV s^{-1} scan rate. **b,** Photocurrent density at +1.23 V$_{RHE}$ extracted from the current–voltage curves. **c,** Change in OCP (vs. RHE) values upon switching off illumination of different intensities. **d,** Current-voltage scans of PM6:D18:L8-BO organic solar cells at different light intensities and 40 mV s^{-1} scan rate. **e,f,** Light intensity dependence of short-circuit current density (**e**) and open circuit voltage (**f**) on the organic solar cells.

Considering the exact same composition and structure of the devices, the distinctly different light intensity dependence points to the photoanode/electrolyte interface as the origin of increased recombination. In a solar cell there is barrier-free extraction of charges even at low charge carrier densities. However, photoanode charge extraction (*i.e.*, injection into the electrolyte) happens only via multiple reaction steps of water oxidation and oxygen evolution involving 4 electrons per O_2 molecule. The HOMO of the polymer donors lies only 150 mV deeper compared to the water oxidation potential (at pH 14 as used here). This means that at low illumination intensities the quasi-Fermi level of photogenerated holes will be shallower than the oxidation potential of water, providing insufficient driving force for the chemical reaction, leading to charge accumulation and to the observed increase in recombination. Application of deeper energy level photoactive materials (especially deeper HOMO of the donor) in organic photoanodes could potentially reduce such recombination at lower light intensities.

Stability of organic photoanodes

The developed graphite-protected PM6:D18:L8-BO photoanodes were tested in lab ambient conditions and under different operational conditions in order to understand the degradation mechanism and improve their stability. The high initial j_{ph} at +1.23 V_{RHE} applied potential was found to decay linearly after the first 0.5 h at a rate of –1.5 mA cm^{-2-} h^{-1} under 1 sun illumination, which slowed down to –0.5 mA cm^{-2} h^{-1} when applying a UV filter (Fig. 4a). This detrimental UV light-driven degradation has been widely reported and assigned to degradation of the BHJ photoactive layer triggered by the adjacent, irradiated oxide transport layers such as TiO_2. This light-induced degradation is reduced, but still present with SnO_2 ETL.[27–29] Measurement of the photoanodes as solar cells for 8 h under continuous illumination (without UV filter) showed around 15% decay of the initial photocurrent (Fig. 4b and Supplementary Fig. 14). The PEC and solar cell stability results suggest that a significant amount of j_{ph} decay originates from the photoinduced degradation of the organic photoactive layer and not from the graphite sheet interface or the presence of aqueous electrolyte. Photoluminescence (PL) spectra recorded after 72 h of PEC operation within and outside the active area further confirm the degradation of the organic absorber layer (Fig. 4c). The active area is defined as the area illuminated (back side) and in contact with electrolyte (front side) during operation. The area outside the active area was kept dry and not illuminated, with just exposure to indoor air and humidity (Supplementary Fig. 15). In both areas the emission is dominated by L8-BO (880 nm) due to effective energy transfer to the narrower bandgap component, although a small contribution from polymer emission can also be observed at 650-700 nm. Within the active area, L8-BO emission is red-shifted, and a slight increase in polymer emission is seen. The red-shift suggests enhanced acceptor crystallinity and taken together with the increased polymer emission is indicative of phase separation between L8-BO acceptor and polymer donor. Such phase separation leads to a less intermixed blend morphology, which will in turn reduce charge generation, possibly leading to the loss of current observed. The fresh photoanodes before operation show no PL peak shift between the different areas of the device, confirming the PL changes observed are due to prolonged photoexcitation of the device (Supplementary Fig. 15).[30,31] It should also be noted that both PM6 and D18 have been shown to degrade rapidly in OPV devices under ambient operation; however, these signatures are often only apparent after longer degradation times than studied here.[32] To look for this degradation pathway, the Raman spectra of the fresh and aged devices were also obtained and no differences were observed (Supplementary Fig. 16), confirming excellent photochemical stability of organic photoanode materials. Therefore, the morphological instability of these organic blend photoanodes is considered as the main mechanism affecting PEC operational stability.

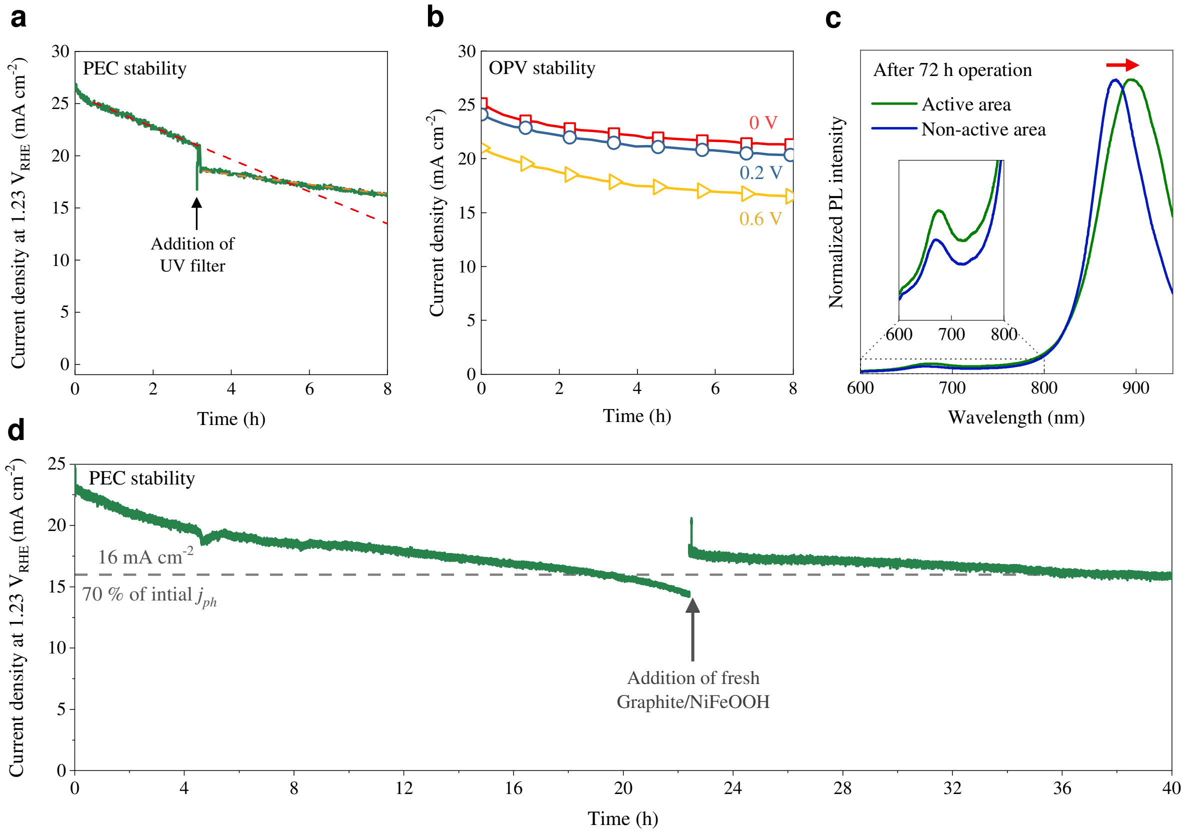

Fig. 4 | Operational stability of PM6:D18:L8-BO organic photoanodes and solar cells at ambient conditions. a, Comparison of operational photocurrent stability of the organic photoanode at +1.23 V_{RHE} under 1 sun illumination without and with a 420 nm cut-off UV filter. Red dashed lines show linear fits to the two phases of photocurrent decay. **b,** Photocurrent stability of the organic photoanode measured as solar cell under continuous illumination without UV filter. **c,** Normalized PL spectra of the photoactive layer of a full organic photoanode after 72 h of continuous PEC operation at +1.23 V_{RHE}. The red arrow indicates the shift in peak position between the PL spectra recorded within the $0.28\ cm^2$ active area (illuminated under operation) and outside of the active area (not illuminated). The inset shows the PL spectra zoomed in on the polymer emission. **d,** Operational photocurrent stability of the organic photoanode for 40 h under 1 sun illumination at +1.23 V_{RHE} with the use of a 420 nm cut-off UV filter. After 22 h operation, a freshly prepared NiFeOOH-functionalized graphite sheet was added. The PEC measurements were performed in an aqueous 1 M NaOH electrolyte.

The developed PM6:D18:L8-BO photoanodes showed an unprecedented 40 h long operational water oxidation stability at +1.23 V_{RHE} with j_{ph} maintained at or above 16 mA cm^{-2} (70% of initial j_{ph}). Such long stability was achieved by application of UV filter and the addition of a new catalyst-functionalized graphite sheet on top of the first one after 22 h of operation (Fig. 4d). The results allow the identification of four phases of photoanode degradation: A first burn-in phase is followed by a second mostly linear j_{ph} decay related to the morphological instability of the photoactive layer as discussed above (Fig. 4a). Third, an accelerated decay (after around 16 h in Fig. 4d) is likely due to the loss of some NiFeOOH from the surface of the graphite sheet, which was reported previously.[22] This is corroborated by the j_{ph} recovering from 14.5 to 18 mA cm^{-2} after the addition of a graphite sheet with freshly electrodeposited NiFeOOH. Fourth, if the graphite sheet is not replaced or covered with a new one, the final phase occurs, which is the non-reversible, fast degradation (reportedly due to delamination of the otherwise photochemically stable organic materials) by the aqueous electrolyte reaching the organic BHJ layer through the deteriorated graphite sheet (Supplementary Fig. 17 and Supplementary Fig. 18).[14] This catastrophic degradation was circumvented by repeated addition of a new graphite sheet upon signs of deterioration, which allowed demonstration of operational stability over 2 days (Supplementary Fig. 17). Alternatively, applying a combination of a denser (15% porosity) non-functionalized graphite sheet and a less dense (50% porosity) NiFeOOH-functionalized top graphite sheet allowed for 3 days long continuous water oxidation by the organic photoanodes (Supplementary Fig. 17). Recording the polarization curve of the photoanode before and after 3 days of solar water splitting reveals 38% reduction of j_{ph} at +1.23 V_{RHE}, but only small change in the E_{on} (from +0.68 V_{RHE} to +0.62 V_{RHE}), further confirming that the operation of the photoanode is not limited by the catalytic activity, but mainly dependent on the morphological instability of the organic BHJ layer (Supplementary Fig. 19).

Comparison to state-of-the-art water-oxidation photoanodes

Fig. 5 displays a comparison of j_{ph} at +1.23 V_{RHE} reported for state-of-the-art water oxidation photoanodes, without using any sacrificial agent. Most of the organic photoanodes until this work generated j_{ph} below 5 mA cm^{-2} apart from one report demonstrating 15 mA cm^{-2}.[14,16,17] The highest j_{ph} of the PM6:D18:L8-BO and PM6:PY-IT devices presented in this work (26.4 mA cm^{-2} and 23.7 mA cm^{-2} respectively) mean a significant leap forward, showcasing the first organic photoanodes with j_{ph} above 25 mA cm^{-2}. Importantly, these high j_{ph} values are accompanied by an unprecedented days-long operational PEC water oxidation stability, which is also a large improvement compared to previous organic photoanodes reporting stability of minutes or hours (Supplementary Table 2). Even when compared to photoanodes with different photoactive layers such as perovskites or silicon, the PM6:D18:L8-BO organic photoanode offers one of the highest j_{ph}, closer to the Shockley-Queisser limit of solar cells (Fig. 5a). The only reported photoanodes generating higher j_{ph} are based on silicon photoactive layers, however those show high E_{on} of +0.9 V_{RHE} or above due to their small 1.1 eV bandgap (Fig. 5b).[33,34]

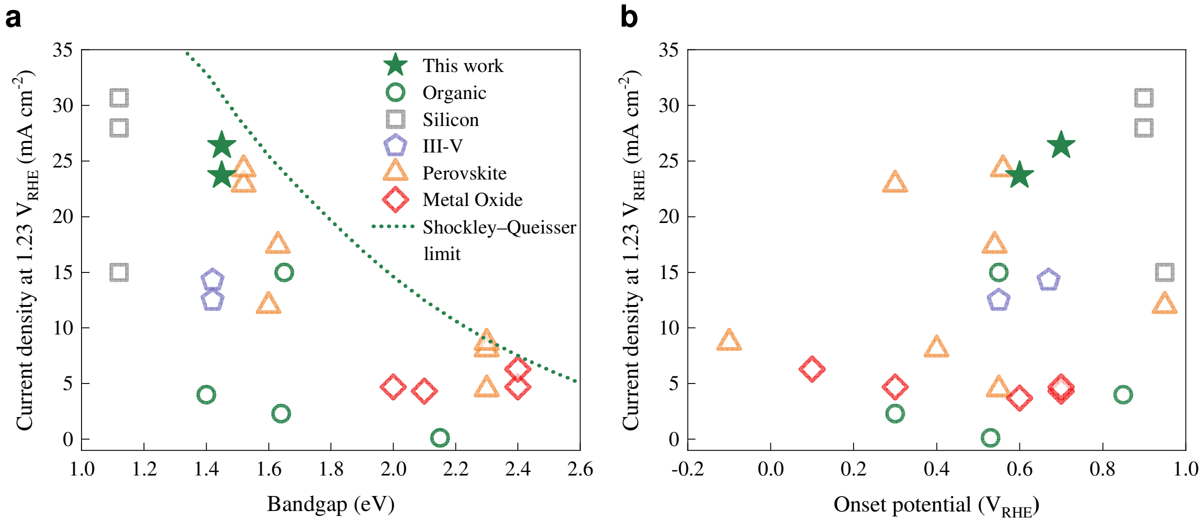

Fig. 5 | Performance comparison of a selection of reported single-junction photoanodes for oxygen evolution reaction without any sacrificial agent. a,b, Comparison of reported photocurrent densities at +1.23 V_{RHE} as a function of the photoactive layer bandgap (**a**) and onset potential for linear rise of photocurrent (**b**). The Shockley-Queisser limit of photocurrent density with different semiconductor bandgaps is shown with green dotted line. Performance parameters and compositions of the compared photoanodes are detailed in Supplementary Table 2.[14,16,17,22,33–49]

Tandem organic photoanodes towards unassisted solar water splitting

Finally, building on the developed single-junction PM6:D18:L8-BO photoanodes, monolithic tandem photoanodes were constructed and are presented here, demonstrating unassisted (*i.e.,* bias-free) solar water splitting using only organic photoactive layers in a single photoelectrode and a platinum counter electrode in the dark (Fig. 6). The tandem cells comprise a wide-bandgap BHJ photoactive layer of GS-ISO, a non-fused non-fullerene acceptor, a low synthetic complexity PTQ10 polymer donor, and PM6:D18:L8-BO as the narrow-bandgap photo-absorber. Upon addition of the NiFeOOH-functionalized graphite sheet, the protected tandem photoanode shows a remarkably low E_{on} of –0.41 V_{RHE} in a three-electrode setup owing to its large photovoltage (Supplementary Fig. 20), which is also reflected in a large ΔOCP value of 1.75 V (Supplementary Fig. 21). This low negative E_{on} allows for unassisted solar water splitting, and tandem photoanodes in two-electrode setup indeed demonstrated j_{ph} of 4.3 mA cm^{-2} at zero applied bias (Fig. 6a), which translates into 5% STH efficiency. The unassisted PEC water splitting was confirmed by the formation of O_2 bubbles on the organic photoanode and H_2 bubbles on the counter electrode (Fig. 6b and Supplementary Video 1). Continuous operation at zero applied bias in two-electrode setup demonstrates the potential of the organic photoanodes for unassisted solar hydrogen generation (Fig. 6b).

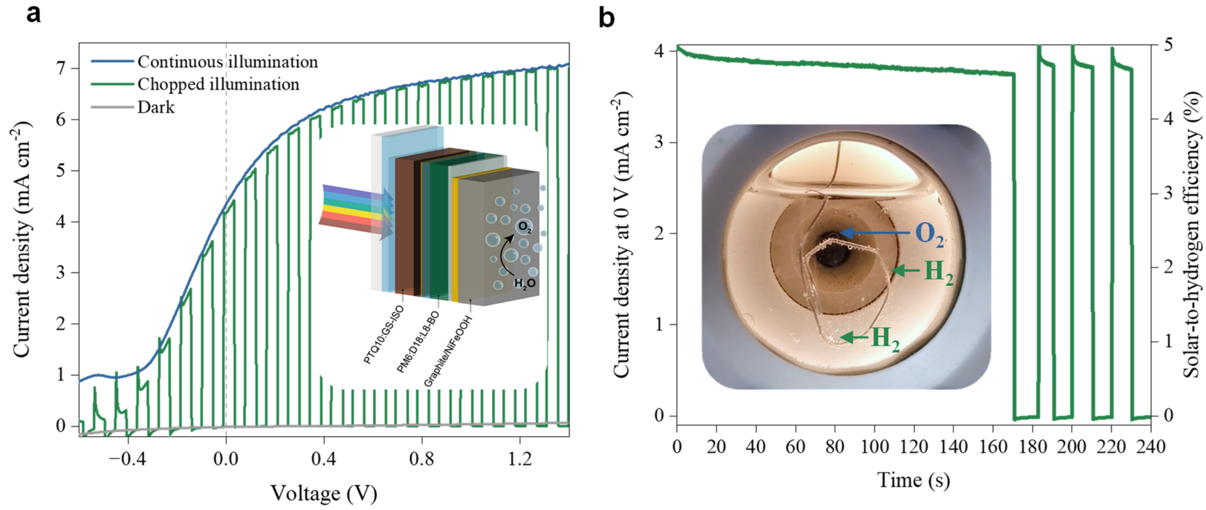

Fig. 6 | Two-electrode PEC performance of the monolithic organic tandem photoanode with PM6:D18:L8-BO and PTQ10:GS-ISO absorber layers. a, Current–voltage scans at 50 mV s^{-1} scan rate in dark, under 1 sun continuous and chopped illumination for the monolithic tandem photoanode in a two-electrode cell with Pt counter electrode. The scan rate for the chopped illumination was 20 mV s^{-1}. Dashed vertical line indicates zero applied potential. The inset displays the schematic structure of the monolithic organic tandem photoanode (not to scale). **b,** Unassisted, two-electrode operational PEC stability of the monolithic organic tandem under continuous (0 – 170 s) and chopped (0 – 240 s) 1 sun illumination. The inset shows a photograph of the tandem photoelectrode in unassisted operation generating O_2 and H_2 bubbles. The measurements were performed in an aqueous 1 M NaOH electrolyte.

Conclusions

The presented BHJ organic photoanodes with PM6:D18:L8-BO photoactive layer demonstrate record photocurrent densities above 25 mA cm^{-2} at +1.23 V_{RHE} and days-long operational photoelectrochemical water-oxidation stability. Such high performance was achieved by the application of an inexpensive graphite sheet functionalized by earth abundant electrocatalyst NiFeOOH that served as a conductive, water-resistant top contact without introducing any electrical losses. The universality of this approach also allowed the fabrication of PM6:PY-IT polymer:polymer organic photoanodes reaching photocurrent densities above 23 mA cm^{-2} at +1.23 V_{RHE} and a reduced onset potential of +0.63 V_{RHE}. Furthermore, monolithic tandem organic photoanodes with PM6:D18:L8-BO and PTQ10:GS-ISO photoactive layers were prepared reaching 5% STH efficiency in a two-electrode setup, which highlights the potential of organic photoanodes for stable, unassisted solar water splitting. Comparison of photoelectrochemical and photovoltaic devices in terms of stability and light intensity dependent performance, as well as photoluminescence measurements of the organic photoactive layer suggest strategies for further improvement of the organic photoanodes: the photostability of the active layer is a key factor to increase the overall stability of the photoanodes, and maintaining large quasi-Fermi level splitting (*i.e.*, illumination above 0.5 sun light intensity) in photoelectrochemical operation is critical to avoid large recombination losses.

Methods

PM6:D18:L8-BO and PM6:PY-IT organic device fabrication. Indium tin oxide (ITO) coated glass substrates were cleaned sequentially in sonication baths of soapy water, water, acetone, and isopropanol (IPA). Tin oxide (SnO_2) nanoparticle ink (Avantama N-31) was spin coated at 3000 rpm onto the cleaned substrates and annealed at 200 °C for 30 min inside a glovebox. PM6 (poly((4,8-bis(5-(2-ethylhexyl)-4-fluoro-2-thienyl)benzo[1,2-b:4,5-b′]dithiophene-2,6-diyl)-2,5-thiophenediyl (5,7-bis(2-ethylhexyl)-4,8-dioxo-4H,8H-benzo[1,2-c:4,5-c′]dithiophene-1,3-diyl)-2,5-thiophenediyl))), D18 (poly (dithieno[3,2-e:2′,3′-g]-2,1,-3-benzothiadiazole-5,8-diyl(4-(2-butyloctyl)-2,5-thiophenediyl)(4,8-bis(5-(2-ethylhexyl)-4-fluoro-2-thienyl)benzo[1,2-b:4,5-b′]dithiophene-2, 6-diyl) (3-(2-butyloctyl)-2,5-thiophenediyl))) and L8-BO (2,2′-((2Z,2′Z)-((3,9-bis(2-butyloctyl)-12,13-bis(2-ethylhexyl)-12,13-dihydro-[1,2,5]thiadiazolo[3,4-e]thieno[2″,3″:4′,5′]thieno[2′,3′:4,5]pyrrolo[3,2g]thieno[2′,3′:4,5] thieno[3,2-b]indole-2,10-diyl)bis(methaneylylidene))bis(5,6-difluoro-3-oxo-2,3-dihydro-1H-indene-2,1-diylidene))dimalononitrile), all from 1-Material, were dissolved at 14 mg mL^{-1} for thin devices or 20 mg mL^{-1} for thick devices in chloroform at weight ratios of 0.8:0.2:1.2, respectively, with 50 % by total weight added diodobenzene (DIB), and stirred for 2 h at 50 °C. The precursor solution was then spin coated at 3000 rpm and annealed at 85 °C for 10 min on a hot plate to form the photoactive layers inside a glovebox. For PM6:PY-IT devices, PM6 and PY-IT (poly[(2,2'-((2Z,2'Z)-((12,13-bis(2-octyldodecyl)-3,9-diundecyl-12,13-dihydro[1,2,5]thiadiazolo[3,4e]thieno[2″,3″:4′,5′]thieno[2′,3′:4,5] pyrrolo[3,2-g]thieno[2′,3′:4,5]thieno[3,2-b]-indole-2,10-diyl)bis(methanylylidene))bis(5-methyl-3-oxo -2,3-dihydro-1H-indene-2,1-diylidene))dimalononitrile-co-2,5-thiophene) from Solarmer were dissolved at a weight ratio of 1:1.2, respectively, at 18 mg mL^{-1} in chloroform, with 1% added chloronaphtalene, spin-coated at 1,700 rpm for 30 s and annealed at 100 °C for 10 min. After PM6:D18:L8-BO or PM6:PY-IT deposition, subsequently 10 nm of MoO_3 and 30 nm of gold (for photoanodes) or 100 nm of silver (for solar cells) were evaporated on top of the active layers.

PTQ10:GS-ISO and PM6:D18:L8-BO tandem organic device fabrication. PTQ10 (poly[[6,7-difluoro[(2-hexyldecyl)oxy]-5,8-quinoxalinediyl]-2,5-thiophenediyl]])) and GS-ISO[50] from 1-Material were dissolved overnight at 20 mg mL^{-1} in chloroform at a weight ratio of 1:1.5, respectively. The solution was spin-cast at 3,000 rpm for 30 s onto ITO-coated glass/SnO_2 substrates and annealed at 145 °C for 25 min. Next, the samples were pre-heated at 120 °C, and BM-HTL-1 (Brilliant Matters),

https://doi.org/10.26434/chemrxiv-2024-vshsx **ORCID:** https://orcid.org/0000-0001-9920-3657 Content not peer-reviewed by ChemRxiv. **License:** CC BY-NC-ND 4.0

previously sonicated and filtered, was spin-cast at 3000 rpm for 50 s, followed by drying for 5 min at 100 °C. Subsequently, 1 nm of gold was evaporated, SnO_2 N-31 ink was spin-cast at 3000 rpm for 30 s and annealed at 145 °C for 10 min in a glovebox, and D18:PM6:L8-BO, MoO_3 and gold were deposited sequentially as described above.

Organic photoanode fabrication. The devices were protected for photoanode use by manually attaching on top of the thin metal electrode of the OPV one or more graphite sheet(s) with an acrylic adhesive layer on the back side and NiFeOOH on the top side. An 0.070 mm graphite sheet (self-adhesive, RS, Panasonic, 1000 W m^{-1} K^{-1}, 115 mm × 90 mm) was applied and in some cases combination of a 0.025 mm thick (self-adhesive, 1600 W m^{-1} K^{-1}, 115 mm × 90 mm) and 0.150 mm thick graphite sheets was used, as stated in figure captions. The NiFeOOH was previously electrodeposited on the graphite sheet(s) using an aqueous solution of 40 mM of nickel sulfate hexahydrate (Sigma-Aldrich, ≥98%) and 10 mM of iron sulfate heptahydrate (Sigma-Aldrich, ≥99%), purged with N_2 for 30 min. A three-electrode setup with platinum counter electrode and Ag/AgCl reference electrode was used for the electrodeposition. The potential was swept from +0.6 to +1.0 $V_{Ag/AgCl}$ at 20 mV s^{-1} scan rate until the electrodeposition charge density reached 4.2 mC cm^{-2}.

Optoelectronic characterization. Shimadzu UV-2600 spectrophotometer was used to obtain the UV-vis spectra of the thin organic layers deposited on ITO-coated glass. Electroluminescence (EL) spectra were obtained using a 2450 Keithley source-meter and a Shamrock 303 spectrograph and iDUS InGaAs array detector (Andor SR 303i-B, cooled to -90 °C). The bandgaps of individual materials and blends were calculated using the intersection between absorption and emission spectra.

Photoluminescence (PL) and Raman spectroscopy measurements on fresh and degraded devices were carried out at different sample positions using a Renishaw in Via Raman microscope with a 50x objective in backscattering configuration. A holographic notch filter was used to remove Rayleigh scattered light. A diffraction grating of 2400 L mm^{-1} was used for Raman measurements, and a grating of 300 L mm^{-1} used for PL measurements. The laser spot ($d = \sim 10$ µm) was focused on to the photoactive layer through the glass substrate and the power was adjusted to give an adequate signal whilst avoiding laser induced degradation; laser power was maintained between samples to allow for comparison. During measurement samples were held in a Linkam stage under a flow of nitrogen to inhibit photooxidation.

(Photo)electrochemical and solar cell measurements. The (photo)electrodes were characterized in a three-electrode setup using an Ivium Compacstat potentiostat, platinum counter electrode, KCl-saturated Ag/AgCl reference electrode and an aqueous 1 M sodium hydroxide electrolyte. Lot Quantum Design xenon lamp was applied as illumination source with an AM 1.5G filter and a circular mask with an area of 0.28 cm^2. 1 sun (100 mW cm^{-2}) irradiance was calibrated by a certified International Light Technologies SEL623 photodetector. The equation $V_{RHE} = V_{Ag/AgCl} + 0.0592 \times \text{pH} + 0.1976$ was used to convert the potentials applied versus the Ag/AgCl reference electrode ($V_{Ag/AgCl}$) to applied potentials versus the reversible hydrogen electrode (V_{RHE}). The potential of the reference electrode ($V_{Ag/AgCl}$) was 0.1976 V versus the standard hydrogen electrode. The current–voltage scans of the graphite sheets attached to glass substrates with and without the NiFeOOH catalyst were recorded with the same setup without illumination. Two-electrode (photo)electrochemical measurements of the tandem photoanodes were performed with the same setup, but with only a counter (platinum) and working electrode connection unless stated differently. Both the PEC and OPV devices were scanned from forward to reverse bias (reverse scan). The photoelectrodes were also characterized as solar cells using a Keithley 2400 source-voltmeter and Newport Oriel solar simulator. Solar cell degradation was studied at ambient conditions with 10 mV s^{-1} scan rate.

The operational PEC photocurrent stability of photoanodes was measured under continuous 1 sun illumination, at an applied bias of +1.23 V_{RHE} for three-electrode measurements. Pyroscience FireStingO2 fiber-optic oxygen meter with a TROXROB10 oxygen probe and a TDIP temperature sensor was used to measure the amount of oxygen generated. A gastight cell was used, which was purged with nitrogen before the measurement. The amount of dissolved oxygen in the electrolyte was calculated applying Henry's law and added to the amount measured in the overhead space. From the measured amount of oxygen and the theoretical amount of oxygen based on the measured photocurrent, the Faradaic efficiency was calculated. MSH-300F LOT Quantum Design monochromator was used to record the photocurrents generated under selected wavelength illumination and calculate IPCE. The intensity of the monochromatic light was measured using a certified International Light Technologies SEL033/U photodetector, which allowed to obtain IPCE spectra in the 300–1000 nm range.

Energy level measurements. The cube root photoemission of the samples was measured by ambient photoemission spectroscopy (APS, KP Technology, SKP5050) and extrapolated to zero, in order to determine the E_v values of the thin layers. Monochromatic UV light irradiation was scanned in the 4.4-6.4 eV range. Kelvin probe measurements were used to record contact potential difference between the tip and the sample. A cleaned silver reference was used to calibrate the tip work function, which then allowed to determine the Fermi level of the samples taking into account the measured contact potential difference of the samples and the work function of the tip. The deep E_v of SnO_2 was not measured, instead previously reported value was used.[27]

References

1. Lewis, N. S. & Nocera, D. G. Powering the planet: Chemical challenges in solar energy utilization. *Proc Natl Acad Sci U S A* **103**, 15729–15735 (2006).
2. Pinaud, B. A. *et al.* Technical and economic feasibility of centralized facilities for solar hydrogen production via photocatalysis and photoelectrochemistry. *Energy Environ Sci* **6**, 1983–2002 (2013).
3. Shaner, M. R., Atwater, H. A., Lewis, N. S. & McFarland, E. W. A comparative technoeconomic analysis of renewable hydrogen production using solar energy. *Energy Environ Sci* **9**, 2354–2371 (2016).
4. van der Spek, M. *et al.* Perspective on the hydrogen economy as a pathway to reach net-zero CO2 emissions in Europe. *Energy Environ Sci* **15**, 1034–1077 (2022).

5. Schneidewind, J. & Schneidewind, J. How Much Technological Progress is Needed to Make Solar Hydrogen Cost-Competitive? *Adv Energy Mater* **12**, 2200342 (2022).
6. Moss, B., Babacan, O., Kafizas, A. & Hankin, A. A Review of Inorganic Photoelectrode Developments and Reactor Scale-Up Challenges for Solar Hydrogen Production. (2021) doi:10.1002/aenm.202003286.
7. Zhang, G. *et al.* Renewed Prospects for Organic Photovoltaics. *Chem Rev* **122**, 14180–14274 (2022).
8. Espinosa, N., Hösel, M., Angmo, D. & Krebs, F. C. Solar cells with one-day energy payback for the factories of the future. *Energy Environ Sci* **5**, 5117–5132 (2012).
9. Zhu, L. *et al.* Single-junction organic solar cells with over 19% efficiency enabled by a refined double-fibril network morphology. *Nature Materials 2022 21:6* **21**, 656–663 (2022).
10. Cho, H. H. & Sivula, K. Advancing operational stability and performance of organic photoanodes for solar water oxidation. *Trends Chem* **4**, 93–95 (2022).
11. Yao, L. *et al.* Organic Semiconductor Based Devices for Solar Water Splitting. *Adv Energy Mater* **8**, 1802585 (2018).
12. Steier, L. & Holliday, S. A bright outlook on organic photoelectrochemical cells for water splitting. *J Mater Chem A Mater* **6**, 21809–21826 (2018).
13. Zhang, D. *et al.* An Organic Semiconductor Photoelectrochemical Tandem Cell for Solar Water Splitting. *Adv Energy Mater* **12**, 2202363 (2022).
14. Cho, H. H. *et al.* A semiconducting polymer bulk heterojunction photoanode for solar water oxidation. *Nature Catalysis 2021 4:5* **4**, 431–438 (2021).
15. Yao, L. *et al.* Establishing Stability in Organic Semiconductor Photocathodes for Solar Hydrogen Production. *J Am Chem Soc* **142**, 7795–7802 (2020).
16. Ho Lee, T. *et al.* A Dual Functional Polymer Interlayer Enables Near-Infrared Absorbing Organic Photoanodes for Solar Water Oxidation. *Adv Energy Mater* **12**, 2103698 (2022).
17. Yu, J. M. *et al.* High-performance and stable photoelectrochemical water splitting cell with organic-photoactive-layer-based photoanode. *Nat Commun* **11**, 1–9 (2020).
18. Thangamuthu, M. *et al.* Polymer Photoelectrodes for Solar Fuel Production: Progress and Challenges. *Chem Rev* **122**, 11778–11829 (2022).
19. Kirner, J. T. & Finke, R. G. Water-oxidation photoanodes using organic light-harvesting materials: a review. *J Mater Chem A Mater* **5**, 19560–19592 (2017).
20. Wang, L. *et al.* Improved Stability and Performance of Visible Photoelectrochemical Water Splitting on Solution-Processed Organic Semiconductor Thin Films by Ultrathin Metal Oxide Passivation. *Chemistry of Materials* **30**, 324–335 (2018).
21. Steier, L. *et al.* Stabilizing organic photocathodes by low-temperature atomic layer deposition of TiO2. *Sustain Energy Fuels* **1**, 1915–1920 (2017).
22. Daboczi, M. *et al.* Scalable All-Inorganic Halide Perovskite Photoanodes with >100 h Operational Stability Containing Earth-Abundant Materials. *Advanced Materials* 2304350 (2023) doi:10.1002/ADMA.202304350.
23. Fehr, A. M. K. *et al.* Integrated halide perovskite photoelectrochemical cells with solar-driven water-splitting efficiency of 20.8%. *Nature Communications 2023 14:1* **14**, 1–12 (2023).
24. Rühle, S. Tabulated values of the Shockley-Queisser limit for single junction solar cells. *Solar Energy* **130**, 139–147 (2016).
25. Street, R. A., Krakaris, A. & Cowan, S. R. Recombination Through Different Types of Localized States in Organic Solar Cells. *Adv Funct Mater* **22**, 4608–4619 (2012).
26. Ma, L. K. *et al.* High-Efficiency Indoor Organic Photovoltaics with a Band-Aligned Interlayer. *Joule* **4**, 1486–1500 (2020).
27. Bai, Y. *et al.* Interfacial engineering and optical coupling for multicolored semitransparent inverted organic photovoltaics with a record efficiency of over 12%. *J Mater Chem A Mater* **7**, 15887–15894 (2019).
28. Luke, J. *et al.* A Commercial Benchmark: Light-Soaking Free, Fully Scalable, Large-Area Organic Solar Cells for Low-Light Applications. *Advanced Energy Materials* vol. 11 2003405 Preprint at https://doi.org/10.1002/aenm.202003405 (2021).
29. Di Mario, L. *et al.* Outstanding Fill Factor in Inverted Organic Solar Cells with SnO2 by Atomic Layer Deposition. *Advanced Materials* 2301404 (2023) doi:10.1002/ADMA.202301404.
30. Luke, J. *et al.* Strong Intermolecular Interactions Induced by High Quadrupole Moments Enable Excellent Photostability of Non-Fullerene Acceptors for Organic Photovoltaics. *Adv Energy Mater* **12**, 2201267 (2022).

31. Razzell-Hollis, J., Limbu, S. & Kim, J. S. Spectroscopic Investigations of Three-Phase Morphology Evolution in Polymer: Fullerene Solar Cell Blends. *Journal of Physical Chemistry C* **120**, 10806–10814 (2016).
32. Wang, Y. *et al.* The critical role of the donor polymer in the stability of high-performance non-fullerene acceptor organic solar cells. *Joule* **7**, 810–829 (2023).
33. Zhou, X. *et al.* Interface engineering of the photoelectrochemical performance of Ni-oxide-coated n-Si photoanodes by atomic-layer deposition of ultrathin films of cobalt oxide. *Energy Environ Sci* **8**, 2644–2649 (2015).
34. Yu, X. *et al.* NiFe Alloy Protected Silicon Photoanode for Efficient Water Splitting. *Adv Energy Mater* **7**, 1601805 (2017).
35. Liu, G., Chen, C., Ji, H., Ma, W. & Zhao, J. Photo-electrochemical water splitting system with three-layer n-type organic semiconductor film as photoanode under visible irradiation. *Sci China Chem* **55**, 1953–1958 (2012).
36. Wang, S. *et al.* Synergistic crystal facet engineering and structural control of WO3 films exhibiting unprecedented photoelectrochemical performance. *Nano Energy* **24**, 94–102 (2016).
37. Kim, J. Y. *et al.* Single-crystalline, wormlike hematite photoanodes for efficient solar water splitting. *Scientific Reports 2013 3:1* **3**, 1–8 (2013).
38. Peerakiatkhajohn, P. *et al.* Stable Hematite Nanosheet Photoanodes for Enhanced Photoelectrochemical Water Splitting. *Advanced Materials* **28**, 6405–6410 (2016).
39. Cui, J. *et al.* 2D Bismuthene as a Functional Interlayer between BiVO4 and NiFeOOH for Enhanced Oxygen-Evolution Photoanodes. *Adv Funct Mater* **32**, (2022).
40. He, B. *et al.* General and Robust Photothermal-Heating-Enabled High-Efficiency Photoelectrochemical Water Splitting. *Advanced Materials* **33**, 2004406 (2021).
41. Poli, I. *et al.* Graphite-protected CsPbBr3 perovskite photoanodes functionalised with water oxidation catalyst for oxygen evolution in water. *Nat Commun* **10**, 1–10 (2019).
42. Yang, H. *et al.* Monolithic FAPbBr3 photoanode for photoelectrochemical water oxidation with low onset-potential and enhanced stability. *Nature Communications 2023 14:1* **14**, 1–13 (2023).
43. Tao, R., Sun, Z., Li, F., Fang, W. & Xu, L. Achieving Organic Metal Halide Perovskite into a Conventional Photoelectrode: Outstanding Stability in Aqueous Solution and High-Efficient Photoelectrochemical Water Splitting. *ACS Appl Energy Mater* **2**, 1969–1976 (2019).
44. Wang, M. *et al.* High-Performance and Stable Perovskite-Based Photoanode Encapsulated by Blanket-Cover Method. *ACS Appl Energy Mater* **4**, 7526–7534 (2021).
45. Choi, H. *et al.* Suppression of Undesired Losses in Organometal Halide Perovskite-Based Photoanodes for Efficient Photoelectrochemical Water Splitting. *Adv Energy Mater* **13**, 2300951 (2023).
46. Kim, T. G. *et al.* Monolithic Lead Halide Perovskite Photoelectrochemical Cell with 9.16% Applied Bias Photon-to-Current Efficiency. *ACS Energy Lett* **7**, 320–327 (2022).
47. Chen, Y. W. *et al.* Atomic layer-deposited tunnel oxide stabilizes silicon photoanodes for water oxidation. *Nature Materials 2011 10:7* **10**, 539–544 (2011).
48. Hu, S. *et al.* Amorphous TiO2 coatings stabilize Si, GaAs, and GaP photoanodes for efficient water oxidation. *Science (1979)* **344**, 1005–1009 (2014).
49. Kang, D. *et al.* Printed assemblies of GaAs photoelectrodes with decoupled optical and reactive interfaces for unassisted solar water splitting. *Nature Energy 2017 2:5* **2**, 1–5 (2017).
50. Bi, P. *et al.* A High-Performance Nonfused Wide-Bandgap Acceptor for Versatile Photovoltaic Applications. *Advanced Materials* **34**, 2108090 (2022).

Acknowledgements

M.D. and S.E. acknowledge the funding of UK Engineering and Physical Sciences Research Council (EPSRC) provided via grant EP/S030727/1. F. E. and J. N. acknowledge financial support from the European Research Council (action no. 742708). M.D. acknowledges support received from Imperial College London, Postdoc and Fellows Development Centre Fund – Seeds for Success (2022). F.E. acknowledges support through the Imperial College Research Fellowship. J.L. and J.S.K. acknowledge the UK EPSRC for the ATIP Programme Grant (EP/T028513/1).

Author contributions

M.D., F.E., J.N. and S.E. conceived, designed, and supervised the project. F.E., S.Y. and N. A. L. fabricated the photoelectrodes, while M.D. performed the photoelectrochemical experiments. J.L. aided with the characterization by Raman spectroscopy. N. A. L. performed the UV-vis spectroscopy. J.S.M. performed the energy level, electroluminescence, light intensity dependent current–voltage, and EQE measurements. M.D. and F.E. wrote the manuscript with the support of J.L., J.N. and S.E. All authors contributed to analyzing and discussing the results.

Competing interests

Competing financial interests: The authors declare no competing financial interests